J. Fluid Mech. (2007), *vol.* 570, *pp.* 155–175.

doi:10.1017/S0022112006003065 Printed in the United Kingdom

Drag and lift forces acting on a spherical water droplet in homogeneous linear shear air flow

By KEN-ICHI SUGIOKA AND SATORU KOMORI

Department of Mechanical Engineering and Science and Advanced Institute of Fluid Science and Engineering, Kyoto University, Kyoto 606-8501, Japan

(Received 6 August 2005 and in revised form 12 June 2006)

Drag and lift forces acting on a spherical water droplet in a homogeneous linear shear air flow were studied by means of a three-dimensional direct numerical simulation based on a marker and cell (MAC) method. The effects of the fluid shear rate and the particle (droplet) Reynolds number on drag and lift forces acting on a spherical droplet were compared with those on a rigid sphere. The results show that the drag coefficient on a spherical droplet in a linear shear flow increases with increasing the fluid shear rate. The difference in the drag coefficient between a spherical droplet and a rigid sphere in a linear shear flow never exceeds 4 %. The lift force acting on a spherical droplet changes its sign from a positive to a negative value at a particle Reynolds number of $Re_p \simeq 50$ in a linear shear flow and it acts from the high-speed side to the low-speed side for $Re_p \geqslant 50$. The behaviour of the lift coefficient on a spherical droplet is similar to that on a stationary rigid sphere and the change of sign is caused by the decrease of the pressure lift. The viscous lift on a spherical droplet is smaller than that on a rigid sphere at the same Re_p, whereas the pressure lift becomes larger. These quantitative differences are caused by the flow inside a spherical droplet.

1. Introduction

The dispersion phenomena of water droplets are often seen in environmental flows with rainfall, clouds, mist, sea spray and so on. It is important to estimate precisely the heat and mass transfer across the air–water interface of a water droplet such as a raindrop falling in the atmosphere or a dispersed droplet over the air–sea interface with intensive wave breaking in developing a reliable climate model. In order to estimate such heat and mass transfer, we have to understand the motions outside and inside a water droplet and the effects of mean shear on fluid forces acting on a water droplet.

When a rigid sphere or a fluid sphere is moving in a shear flow, transverse force is exerted as lift force. According to the inviscid and low-Reynolds-number theories, the lift force acts from the higher fluid velocity side to the lower velocity side (Saffman 1965; Auton 1987; Dandy & Dwyer 1990; McLaughlin 1993). Komori & Kurose (1996) and Kurose & Komori (1999) first performed three-dimensional direct numerical simulation for the flow field outside a rigid sphere in the range of particle Reynolds numbers of $Re_p = 1$–500. Here, Re_p is defined by $U_c d/\nu$, where d is the diameter of a sphere, U_c the fluid velocity on the streamline through the centre of a sphere and ν the kinematic viscosity. They found that the direction of the lift force acting on a stationary rigid sphere at higher Re_p is opposite to that predicted by the inviscid and low-Reynolds-number theories. The same behaviour of the lift force on a stationary rigid sphere was also reported in the direct numerical simulation (DNS) of

Bagchi & Balachandar (2002). On the other hand, the shear lift force on a bubble for high particle Reynolds numbers has been discussed in numerical simulations. Mei & Klausner (1994) obtained an expression of the lift force on an inviscid sphere, i.e. a fluid sphere with non-viscous internal flow, in a linear shear flow by combining the three results for a rigid sphere in a viscous flow obtained by the linear analysis by Saffman (1965), the DNS of Dandy & Dwyer (1990) and the analytical solution of McLaughlin (1993) with the analytical results for a sphere in an inviscid flow obtained by Auton (1987). Legendre & Magnaudet (1998) and Kurose, Misumi & Komori (2001) also computed the lift force acting on an inviscid sphere in a viscous flow by using DNSs.

In those previous studies, only the flow field outside a rigid sphere or an inviscid sphere has been considered in a uniform shear flow. However, in the case of a fluid sphere such as a spherical droplet, it is necessary to consider the flow fields both outside and inside a fluid sphere. For a uniform unsheared creeping flow ($Re_p \ll 1$), the flow fields outside and inside a spherical droplet have been analysed by the Hadamard–Rybczynski solution (see Clift, Grace & Weber 1978). For moderate and high particle Reynolds numbers ($Re_p > 1$), drag coefficient on a droplet in a uniform unsheared flow was estimated only by experiments (Gunn & Kinzer 1949; Beard & Pruppacher 1969), and it was observed that circulating flows inside a spherical droplet are generated by the viscous stress on the surface of a droplet. However, the details of the flow fields outside and inside a droplet have not been clarified. On the other hand, the numerical studies on a spherical droplet for moderate particle Reynolds numbers ($Re_p > 1$) are limited (LeClair *et al.* 1972; Chen 2001). In these studies, the flow fields outside and inside a semicircular droplet were computed under the coarse assumption that flow fields outside and inside a spherical droplet were axisymmetric. However, when vortex shedding appears behind a rigid sphere in a uniform flow in the high-Reynolds-number range, flow structure around a rigid sphere is far from axisymmetric. Therefore, previous numerical studies on a spherical droplet under the coarse assumption of axis-symmetry are not suitable. In previous numerical studies on the dispersion of droplets in the air flow, the assumption that fluid forces on a spherical droplet for moderate Re_p can be approximated by those on a rigid sphere has also been used. However, this assumption has not been verified, since the effect of the flow inside a spherical droplet in a linear shear flow on the fluid forces has not been investigated. Thus, the mean shear effects on the drag and lift forces on a spherical droplet in a shear flow have not been clarified.

The purpose of this study is, therefore, to investigate the effects of the fluid shear on drag and lift forces acting on a spherical water droplet in a viscous linear shear air flow for moderate and high particle Reynolds numbers by applying a three-dimensional direct numerical simulation to flows both inside and outside a droplet, and to clarify the difference in the generation mechanism of lift force between a spherical droplet and a rigid sphere.

2. Direct numerical simulation

The flow geometry and coordinate system for computations are shown in figure 1. The ambient flow around a droplet is a linear shear flow. The three-dimensional Navier–Stokes (NS) equations in cylindrical coordinates are given by

$$\frac{\partial U}{\partial t} + (\boldsymbol{V} \cdot \nabla) U = -\frac{\partial p}{\partial x} + \frac{1}{Re_{p,k}} \nabla^2 U, \tag{2.1}$$

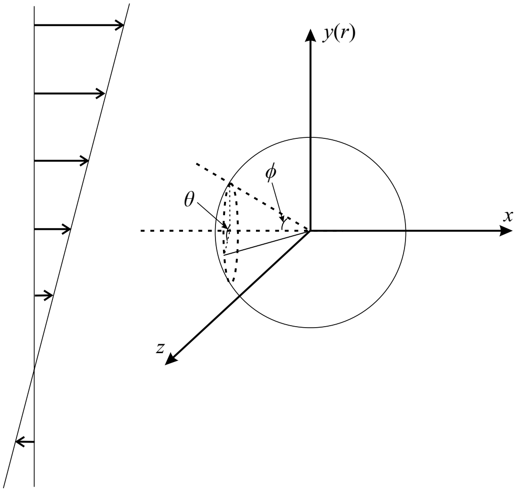

FIGURE 1. Coordinate system for a spherical droplet.

μ_o	1.82×10^{-5} kg m^{-1} s^{-1}
μ_i	8.91×10^{-4} kg m^{-1} s^{-1}
ρ_o	1.19 kg m^{-3}
ρ_i	9.97×10^2 kg m^{-3}

TABLE 1. Fluid properties.

$$\frac{\partial V}{\partial t} + (\boldsymbol{V}\cdot\nabla)V - \frac{V^2}{r} = -\frac{\partial p}{\partial r} + \frac{1}{Re_{p,k}}\left(\nabla^2 V - \frac{V}{r^2} - \frac{2}{r^2}\frac{\partial W}{\partial \theta}\right), \tag{2.2}$$

$$\frac{\partial W}{\partial t} + (\boldsymbol{V}\cdot\nabla)W + \frac{VW}{r} = -\frac{1}{r}\frac{\partial p}{\partial \theta} + \frac{1}{Re_{p,k}}\left(\nabla^2 W - \frac{W}{r^2} + \frac{2}{r^2}\frac{\partial V}{\partial \theta}\right). \tag{2.3}$$

The particle Reynolds number $Re_p(=\rho U_c d/\mu)$ is based on the mean velocity of the fluid on the stream through the centre of the droplet, U_c. Here, ρ is the density of the fluid, d is the diameter of a droplet and μ is the viscosity. The particle Reynolds number outside a droplet, $Re_{p,o}$, and the particle Reynolds number inside a droplet, $Re_{p,i}$, are not independent, and are related by

$$Re_{p,i} = \frac{\rho_i}{\rho_o}\frac{\mu_o}{\mu_i}Re_{p,o}, \tag{2.4}$$

where the subscripts o and i indicate the ambient flow outside a droplet and the flow inside a droplet, respectively. Physical properties of fluids are shown in table 1 and the fluids outside and inside a droplet correspond to air and water. The capillary number $(=\mu U_c/\sigma)$ and the Weber number $(=\rho U_c^2 d/\sigma)$ of a water droplet in the air flow were 1.0×10^{-3} and 0.30 at maximum. Here, σ denotes the surface tension. From these values of the capillary and the Weber number, it is understood that the deformation of the droplet from a spherical shape and the force owing to the deformation are negligibly small (Wohl & Rubinow 1974; Leal 1980).

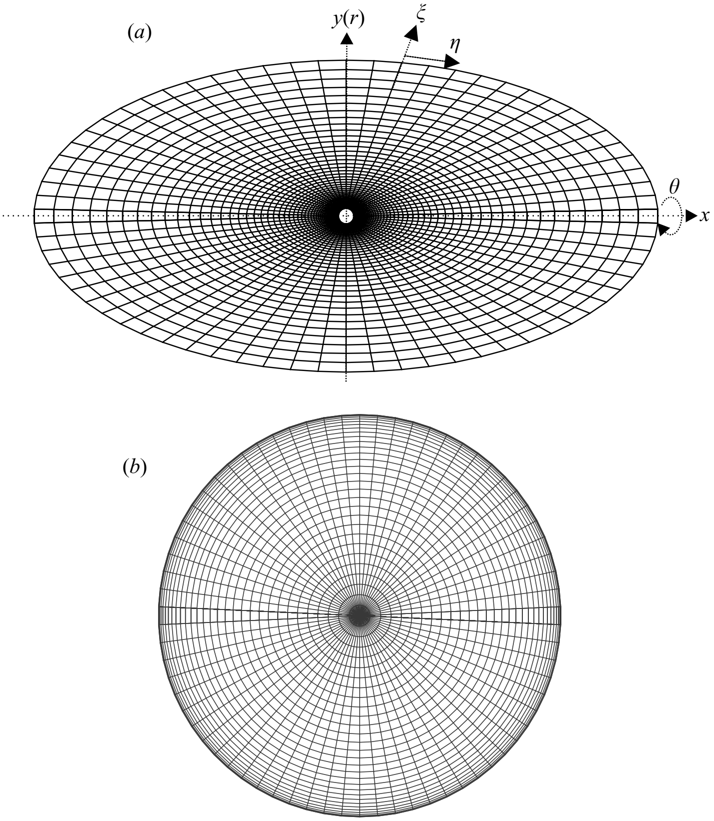

FIGURE 2. Schematic diagram of computational domains: (*a*) outside, (*b*) inside a spherical droplet.

The NS equations were solved directly using a finite-difference scheme based on the marker and cell (MAC) method. The numerical procedure used here was first developed by Hanazaki (1988) and is essentially the same as that used in Komori & Kurose (1996), Kurose & Komori (1999) and Kurose *et al.* (2001). The transformed governing equations were discretized to construct the finite-difference formulation. The nonlinear terms in NS equations were approximated by a third-order scheme of Kawamura & Kuwahara (1984), and other spatial derivatives were approximated by a second-order central difference scheme. The (x, r, θ)-coordinate system was transferred to the (η, ξ, θ)-coordinate system with an equal spacing. Numerical grids outside and inside a spherical droplet are shown in figures 2(*a*) and 2(*b*). In the present study, the size of the computational domain was 20 and 10 diameters in the x- and r-directions, respectively. The size of the computational domain was determined by confirming that the difference in the computed results between the present size and the size of 50 and 25 diameters in the x- and r-directions is less than 2 % for $Re_p \geqslant 5$. It was also confirmed that the small difference does not affect flow structures and drag and lift forces. The grid points outside a droplet used in this study were $35 \times 61 \times 48$ in the η, ξ and θ directions, and the grid points inside a droplet were $35 \times 31 \times 48$. The grid points were determined by confirming that the difference in the computed results between the present grid points and the double grid points is less than 2 %.

The boundary condition of velocity upstream of a spherical droplet was given in a dimensionless form by

$$U = 1 + \alpha y. \tag{2.5}$$

Here, α is the dimensionless fluid shear rate of the mean flow. The velocity condition at the outer boundary, except the upstream, was given by

$$\frac{\partial \boldsymbol{V}}{\partial x} = 0. \tag{2.6}$$

The boundary conditions on the surface of a droplet were given by a no mass flow condition across the interface and continuity of tangential velocities and stresses:

$$v_{n,o} = v_{n,i} = 0, \tag{2.7}$$

$$\tau_{n\theta,o} = \tau_{n\theta,i}, \tag{2.8}$$

$$\tau_{n\phi,o} = \tau_{n\phi,i}, \tag{2.9}$$

$$v_{\theta,o} = v_{\theta,i}, \tag{2.10}$$

$$v_{\phi,o} = v_{\phi,i}. \tag{2.11}$$

Here, the subscript n in the viscous stress τ denotes the normal direction to the surface of a droplet, and θ and ϕ show the tangential directions to the surface of a droplet. Because of the singularity at $r = 0$ in the cylindrical coordinates, the velocity at the centre of a spherical droplet was given by

$$U(x, 0, \theta) = \frac{U(x, \Delta r, \theta) + U(x, \Delta r, \theta + \pi)}{2}. \tag{2.12}$$

In order to compare the fluid forces acting on a spherical droplet with those on a rigid sphere, the air velocity field around a rigid sphere was computed by using the same DNS. In this case, the boundary conditions on the surface of a rigid sphere were given by a non-slip condition. A rigid sphere was fixed and was not rotated.

The drag and lift forces are the components of the fluid force acting on a spherical droplet in the streamwise (x) direction and normal (y) direction to the streamwise direction, F_D and F_L, and they were computed by integrating the pressure and viscous stresses over the surface of a spherical droplet:

$$F_D = F_{D,p} + F_{D,f} = \boldsymbol{e}_x \cdot \int_S -p\boldsymbol{e}_n \, \mathrm{d}S + \boldsymbol{e}_x \cdot \int_S \boldsymbol{\tau} \, \mathrm{d}S, \tag{2.13}$$

$$F_L = F_{L,p} + F_{L,f} = \boldsymbol{e}_y \cdot \int_S -p\boldsymbol{e}_n \, \mathrm{d}S + \boldsymbol{e}_y \cdot \int_S \boldsymbol{\tau} \, \mathrm{d}S. \tag{2.14}$$

Here, $\boldsymbol{e}_x$ and $\boldsymbol{e}_y$ are the unit vectors in the x- and y-direction. The term $\boldsymbol{e}_n$ is the unit normal vector to the surface of a droplet. The first term is the pressure force, while the second term is the viscous force. The drag and lift coefficients, C_D and C_L, are defined by

$$C_D = C_{D,p} + C_{D,f} = \frac{F_{D,p}}{\frac{1}{2}\pi\rho_o U_c^2 (d/2)^2} + \frac{F_{D,f}}{\frac{1}{2}\pi\rho_o U_c^2 (d/2)^2}, \tag{2.15}$$

$$C_L = C_{L,p} + C_{L,f} = \frac{F_{L,p}}{\frac{1}{2}\pi\rho_o U_c^2 (d/2)^2} + \frac{F_{L,f}}{\frac{1}{2}\pi\rho_o U_c^2 (d/2)^2}. \tag{2.16}$$

Here, $C_{D,p}$ and $C_{D,f}$ are the pressure and viscous drag coefficients and $C_{L,p}$ and $C_{L,f}$ are the pressure and viscous lift coefficients, respectively. Computations were repeated with a dimensionless time step of $\Delta t = 0.005$ until almost approaching steady state.

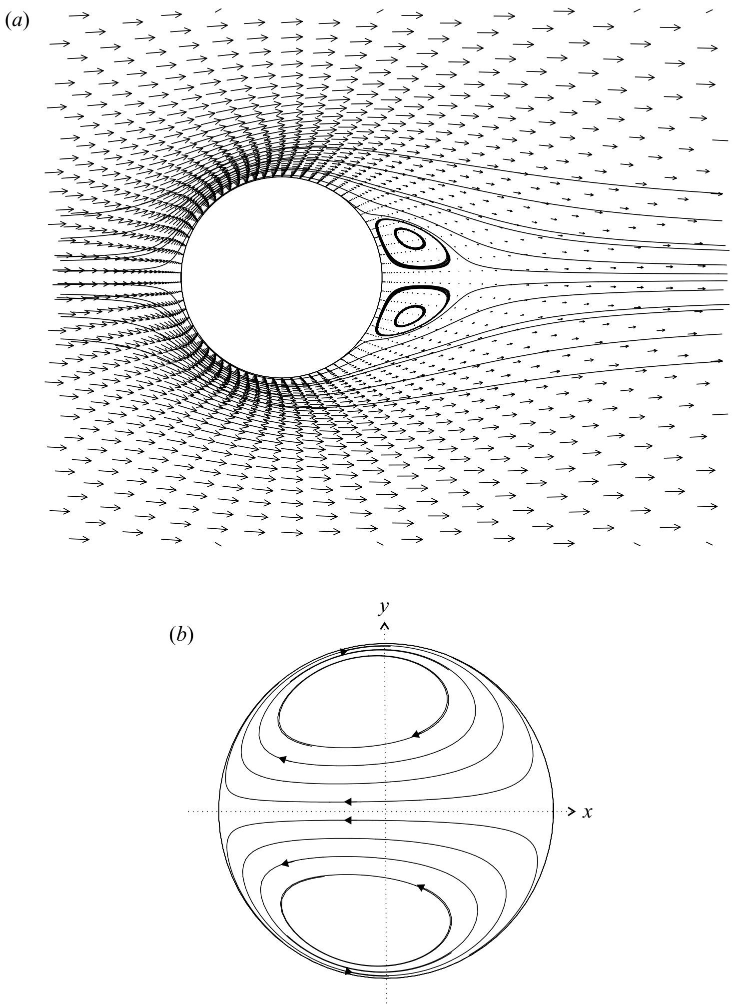

FIGURE 3. Velocity fields and streamlines at $Re_p = 50$ and $\alpha = 0.0$: (a) outside, (b) inside a spherical droplet.

However, the drag and lift forces acting on a spherical droplet with the high particle Reynolds number ($Re_p = 300$) were oscillated by the wake due to the flow separation behind a spherical droplet, and therefore the drag and lift coefficients on a spherical droplet were estimated by taking the time-averaged value over 40 000 time steps. Similarly, the drag and lift forces on a rigid sphere were estimated.

The computations for both a spherical droplet and a rigid sphere were performed for particle Reynolds numbers of $Re_p = 1$, 5, 10, 50, 100 and 300 and for fluid shear rates of $\alpha = 0.0$, 0.1, 0.2, 0.3 and 0.4.

3. Results and discussion

3.1. *Flow fields outside and inside a spherical droplet*

Figure 3 shows the velocity fields and streamlines outside and inside a spherical droplet in a uniform unsheared flow at $Re_p = 50$ and $\alpha = 0.0$ on the centreplane ($z = 0$). It is found that flow separations appear behind a spherical droplet in the ambient air

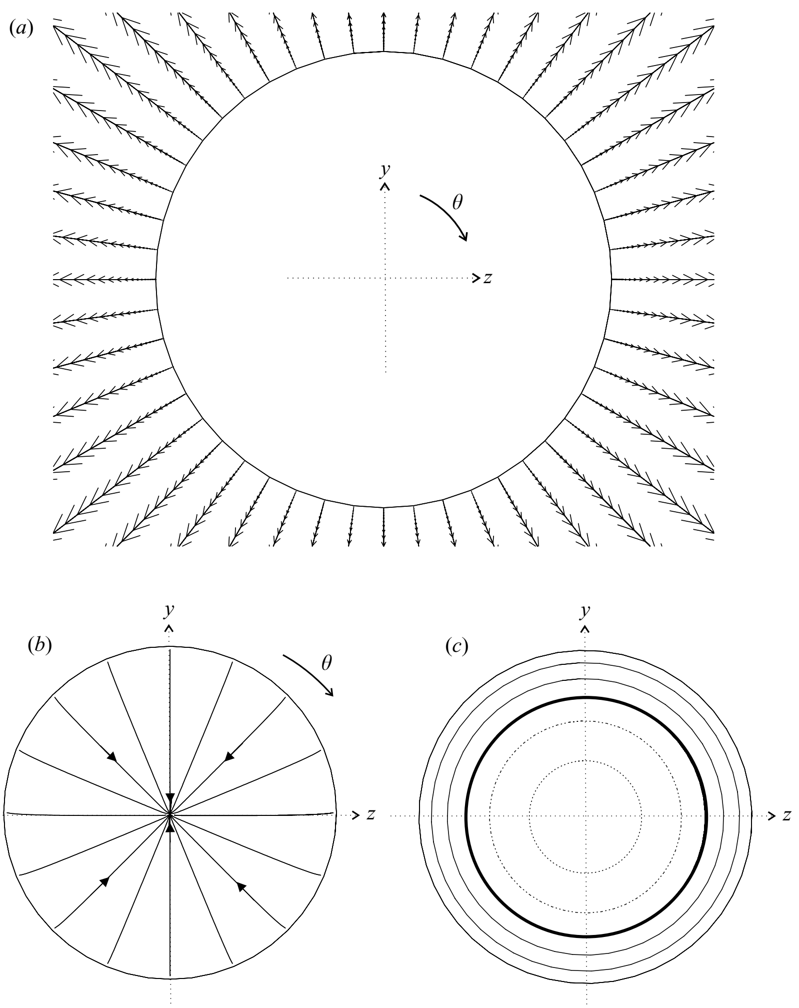

FIGURE 4. Velocity fields and streamlines (*a*) outside, (*b*) inside a spherical droplet and (*c*) the contours of the velocity in the streamwise (x) direction inside a spherical droplet at $Re_p = 50$ and $\alpha = 0.0$ on the (y, z)-plane ($x = 0$). The bold, solid and dotted lines in (*c*) denote the zero, positive and negative values of the velocity in the x-direction.

flow, and internal water circulations inside a spherical droplet are generated by the viscous stress acting on the surface of a droplet. The stagnation points appear at the upstream end and the downstream end of the droplet surface. Figure 4 shows the velocity fields and streamlines outside and inside a spherical droplet in a uniform unsheared flow at $Re_p = 50$ and $\alpha = 0.0$ on the (y, z)-plane ($x = 0$). It is found that streamlines outside and inside a spherical droplet are straight lines normal to the surface of droplets. This shows that the flow in the angular direction (θ-direction) is not generated. The flows in the upstream direction are generated in the central region of a spherical droplet and the flows in the downstream direction are generated near the surface of a spherical droplet. The contour lines of the velocity in the x-direction are circular. This shows that the distribution of the velocity in the x-direction inside a spherical droplet on the (y, z)-plane ($x = 0$) is axisymmetric. Therefore, both air and

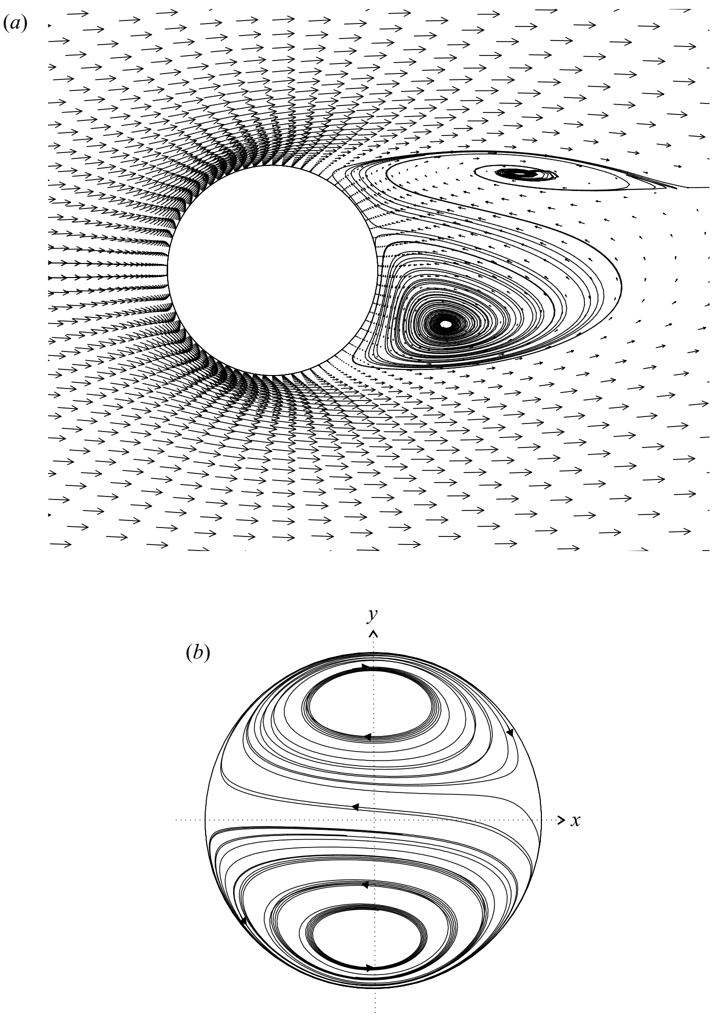

FIGURE 5. Velocity fields and streamlines at $Re_p = 300$ and $\alpha = 0.0$: (*a*) outside, (*b*) inside a spherical droplet.

water flow fields are axisymmetric. Figure 5 shows the velocity fields and streamlines outside and inside a spherical droplet in a uniform unsheared flow at $Re_p = 300$ and $\alpha = 0.0$ on the centreplane ($z = 0$). In this case, the vortex shedding appears in the ambient air flow. Neither air nor water flow fields are axisymmetric. On the other hand, when we perform a three-dimensional DNS by applying the assumption of axisymmetric flow used in previous studies (LeClair *et al.* 1972; Chen 2001), large internal circulations and small secondary circulations inside a spherical droplet appear (figure 6). The directions of the large internal circulations and small secondary circulations are opposite. A similar double-vortex motion inside a droplet has been reported by LeClair *et al.* (1972) and Chen (2001). However, our three-dimensional direct numerical simulation without such an unreal assumption shows that double-vortex motions inside a spherical droplet can never be generated (see figure 5*b*). Figure 7 shows the velocity fields and streamlines outside and inside a spherical droplet in a uniform unsheared flow at $Re_p = 300$ and $\alpha = 0.0$ on the (y, z)-plane

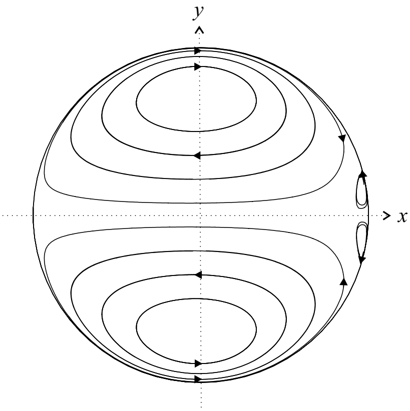

FIGURE 6. Streamlines inside a spherical droplet at $Re_p = 300$ and $\alpha = 0.0$ under the assumption of the axisymmetric flow (LeClair *et al.* 1972; Chen 2001).

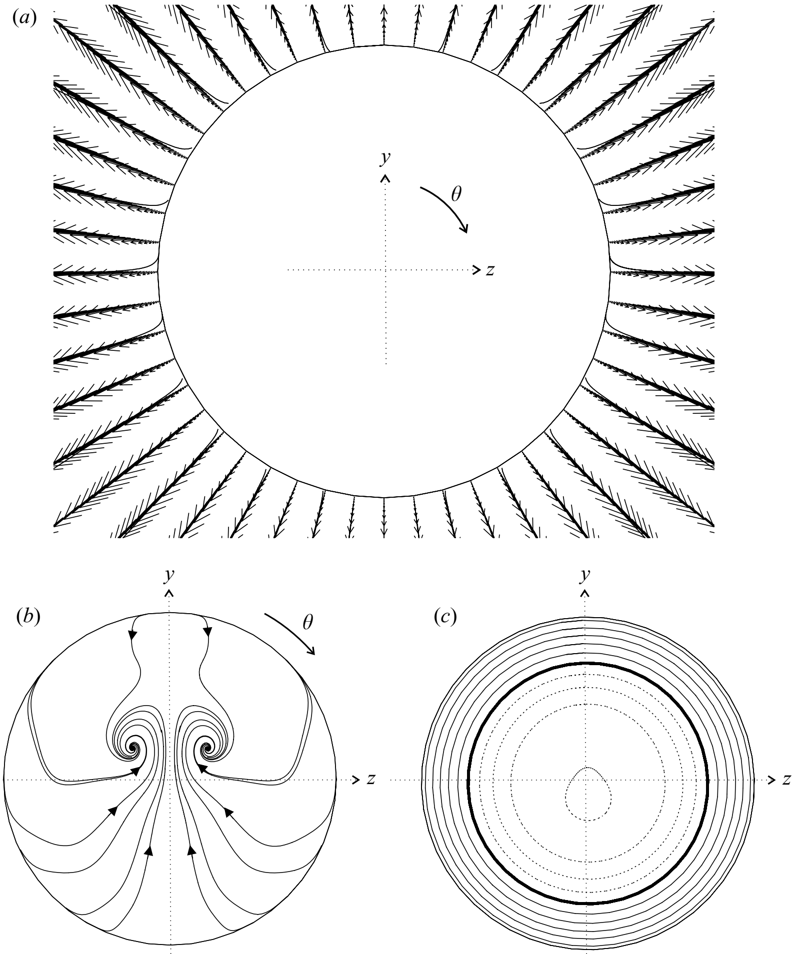

FIGURE 7. Velocity fields and streamlines (*a*) outside, (*b*) inside a spherical droplet and (*c*) the contours of the velocity in the streamwise (x) direction inside a spherical droplet at $Re_p = 300$ and $\alpha = 0.0$ on the (y, z)-plane ($x = 0$). The bold, solid and dotted lines in (*c*) denote the zero, positive and negative value of the velocity in the x-direction.

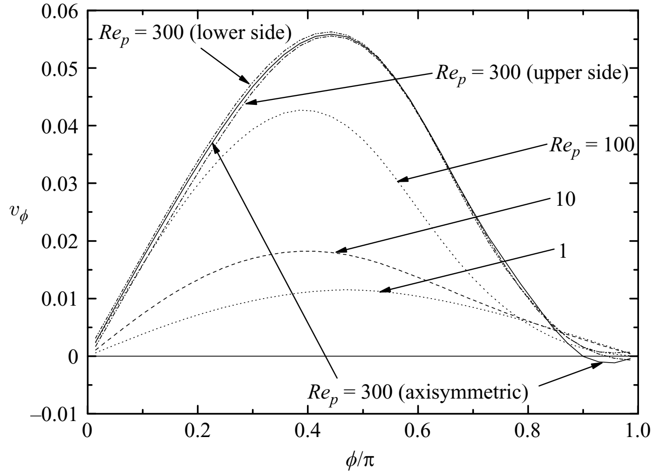

FIGURE 8. Tangential velocity on the surface of a spherical droplet.

($x = 0$). It is found that streamlines are not straight lines perpendicular to the droplet surface both outside and inside a spherical droplet. This shows the flows in the angular direction (θ-direction) are generated both outside and inside a spherical droplet. The upward flows toward the central region of a droplet are generated at the central part of a spherical droplet and the downward flows owing to the flows in the angular direction are also generated near the surface of a spherical droplet. The flows in the upstream direction are generated in the central region of a spherical droplet and the flows in the downstream direction are generated near the surface of a spherical droplet. The contour line of the velocity in the x-direction on the (y, z)-plane is not the circular shape. This shows the distribution of the velocity in the x-direction inside a spherical droplet on the (y, z)-plane ($x = 0$) is not axisymmetric. These three-dimensional flows are quite different from the axisymmetric flow in figure 4. Figure 8 shows the tangential velocity on the surface of a spherical droplet, v_ϕ, on the centreplane ($z = 0$). The values of $\phi = 0$ and $\phi = \pi$ correspond to the upstream end of the droplet surface and the downstream end of the droplet surface, respectively. Flow fields at $Re_p = 300$ and $\alpha = 0.0$ are quasi-steady, and therefore the instantaneous velocities at a time on both the upper and lower surfaces of a droplet are shown in figure 8. It is found that the surface velocity, v_ϕ, increases with increasing Re_p. Under the assumption of the axisymmetric flow, the opposite tangential surface velocity caused by secondary circulations appears near $\phi = \pi$ at $Re_p = 300$, as shown by a solid line. However, such an opposite tangential velocity on both upper and lower surfaces cannot be found in the present three-dimensional flow.

Figure 9 shows the velocity fields and streamlines outside and inside a spherical droplet in a linear shear flow at $Re_p = 50$ and $\alpha = 0.4$ on the centreplane ($z = 0$). It is found that the vortex appears on the lower side in the ambient air flow. Flow fields outside and inside a spherical droplet are three-dimensional, although the symmetry exists on the (x, z)-plane ($y = 0$) as shown in figure 10. Figure 11 shows the velocity fields and streamlines outside and inside a spherical droplet in a linear shear flow at $Re_p = 300$ and $\alpha = 0.4$ on the centreplane ($z = 0$). The velocity field and streamlines are almost similar to those of $Re_p = 50$, although a big difference was observed between $Re_p = 50$ and 300 in a unsheared flow.

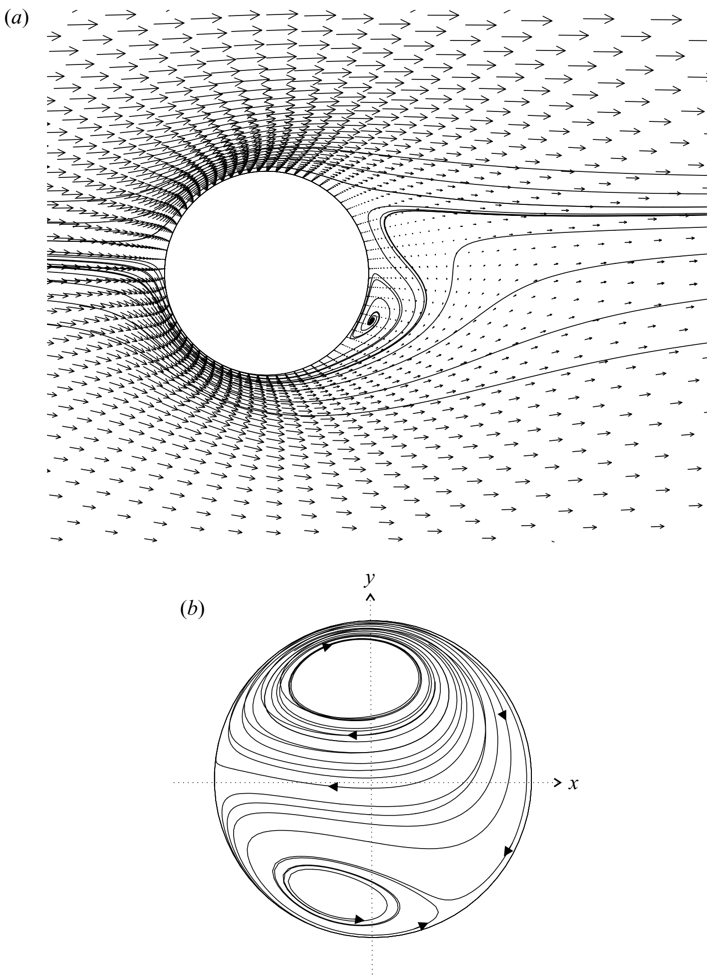

FIGURE 9. Velocity fields and streamlines at $Re_p = 50$ and $\alpha = 0.4$: (*a*) outside, (*b*) inside a spherical droplet.

3.2. *Drag coefficient*

Figures 12 and 13 show the variations of the drag coefficient, C_D, on a rigid sphere and a spherical droplet in a uniform unsheared flow against the particle Reynolds number, Re_p, respectively. The computed C_D on a rigid sphere is compared in figure 12 with the experimental results for a rigid sphere by Morsi & Alexander (1972). The computed C_D on a spherical droplet is also compared in figure 13 with the experimental results for a droplet by Beard & Pruppacher (1969) and Gunn & Kinzer (1949). The present DNS predictions for a rigid sphere and a spherical droplet are in good agreement with their measurements. This supports the reliability of the present DNS. The oscillation of drag and lift forces acting on a spherical droplet with the high particle Reynolds number ($Re_p = 300$) was generated by the wake due to the flow separation behind a spherical droplet. The time variations of the drag and lift coefficients on a spherical droplet at $Re_p = 300$ and $\alpha = 0.0$ are shown in figure 14. The $C_D(t)$ and $C_L(t)$ denote the instantaneous drag and lift coefficients at a dimensionless time, t, respectively. The C_D and C_L are the time-averaged values of drag and lift coefficients, respectively.

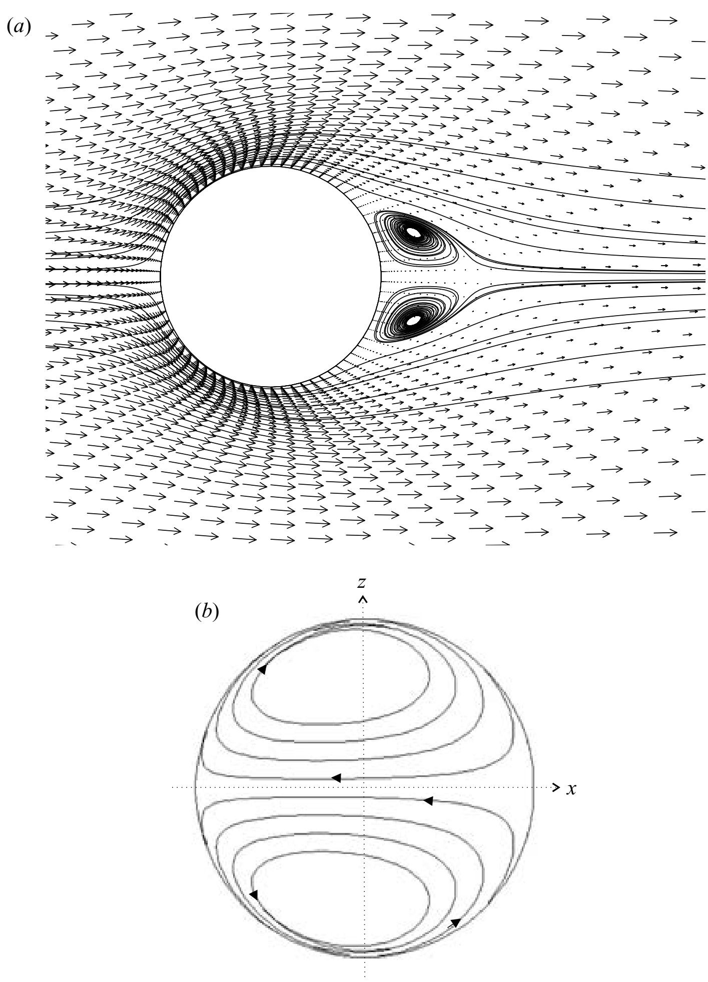

FIGURE 10. Velocity fields and streamlines on the plane of $y = 0$ at $Re_p = 50$ and $\alpha = 0.4$: (a) outside, (b) inside a spherical droplet.

It is found that the fluctuation of the lift coefficient is stronger than that of the drag coefficient. The frequencies of the time variations of the drag and lift coefficients due to the vortex shedding had the same value, and the value of the Strouhal number based on the vortex-shedding frequency $f(St(= df/U_c))$ was estimated to be 0.125. Similarly, the Strouhal number for a rigid sphere was estimated to be the same as for a spherical droplet. The present value of 0.125 is in quantitative agreement with the Sakamoto & Haniu's (1995) experimental result of 0.128 for a rigid sphere. Figure 15 shows the ratio of the drag coefficient on a spherical droplet in a linear shear flow, C_D, to the drag coefficient in a uniform unsheared flow, C_{D0}, against Re_p. The ratio, C_D/C_{D0}, increases with increasing the dimensionless shear rate α for a fixed value of Re_p, and the dependence of C_D on α is more obvious for higher Re_p. To clarify the difference in the drag between a spherical droplet and a rigid sphere, the ratio of the drag coefficient on a spherical droplet, $C_{D,d}$, to that on a rigid sphere, $C_{D,s}$, is plotted against Re_p in figure 16. The difference in the drag between a spherical droplet and a rigid sphere is small and it never exceeds 4 %. However, it is obvious that the drag

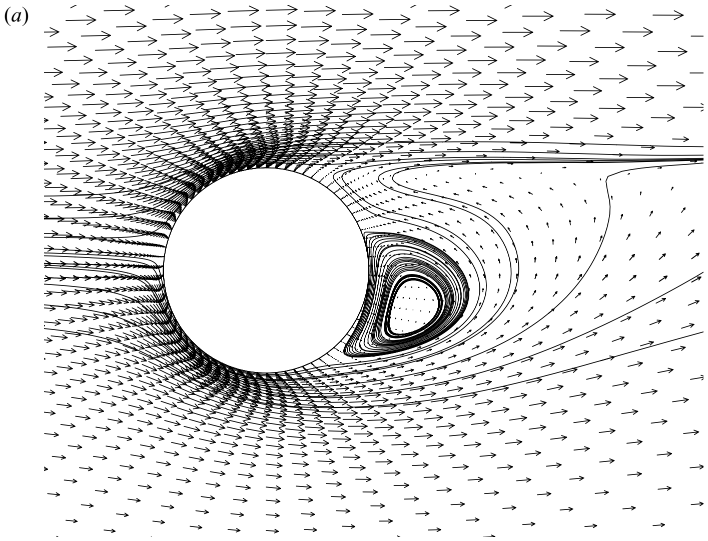

FIGURE 11. Velocity fields and streamlines at $Re_p = 300$ and $\alpha = 0.4$: (a) outside, (b) inside a spherical droplet.

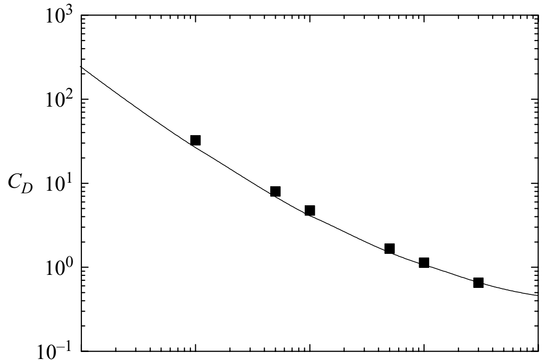

FIGURE 12. Drag coefficient, C_D, on a rigid sphere in a uniform unsheared flow versus the particle Reynolds number, Re_p. —, Morsi & Alexander (1972).

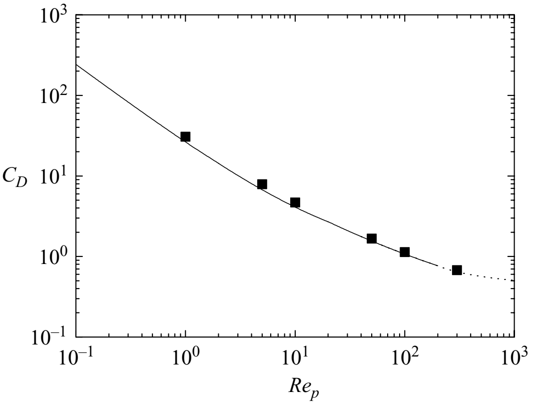

FIGURE 13. Drag coefficient, C_D, on a spherical droplet in a uniform unsheared flow versus the particle Reynolds number, Re_p. —, Beard & Pruppacher (1969); ···, Gunn & Kinzer (1949).

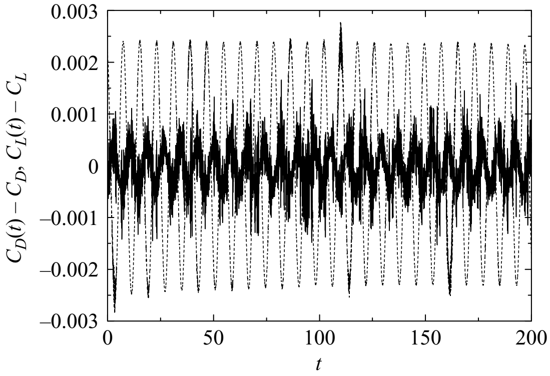

FIGURE 14. The time variations of drag and lift coefficients on a spherical droplet at $Re_p = 300$ and $\alpha = 0.0$; The solid and dashed lines correspond to the drag and lift coefficients, respectively.

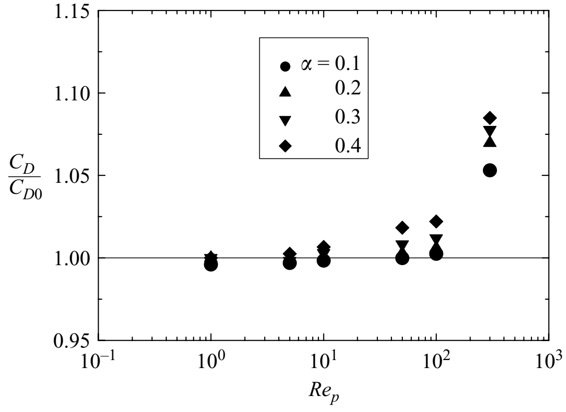

FIGURE 15. The ratio of drag coefficient, C_D, on a spherical droplet in a linear shear flow to that in a uniform unsheared flow, C_{D0}, versus the particle Reynolds number, Re_p.

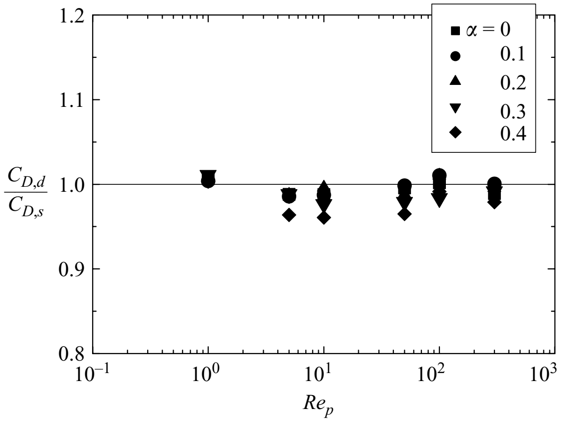

FIGURE 16. The ratio of drag coefficient on a spherical droplet in a linear shear flow, $C_{D,d}$, to that on a rigid sphere, $C_{D,s}$, versus the particle Reynolds number, Re_p.

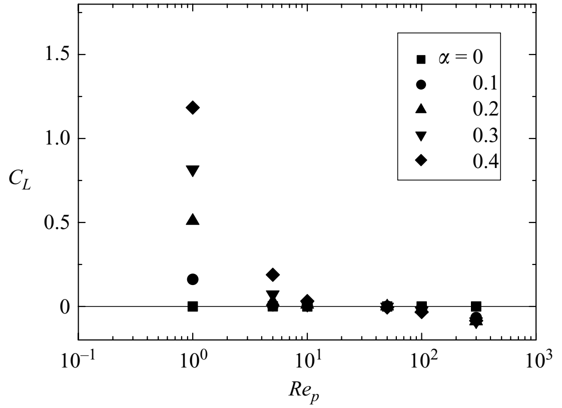

FIGURE 17. Lift coefficient, C_L, on a spherical droplet versus the particle Reynolds number, Re_p.

on a spherical droplet is a little smaller than that on a rigid sphere. In the middle Reynolds-number region where the drag on a spherical droplet is obviously smaller than the drag on a rigid sphere, the ratio of the viscous drag on a spherical droplet to that on a rigid sphere was 0.975, 0.975 and 0.982 at $Re_p = 5$, 10 and 50, respectively. On the contrary, the ratio of the pressure drag on a spherical droplet to that on a rigid sphere was 1.02 at $Re_p = 5$, 10 and 50. These show that the decrease of the drag is caused by the decrease of the viscous drag. The decrease of the viscous drag is due to the presence of the water flow on the droplet surface (see figure 3).

3.3. *Lift coefficient*

Figures 17 and 18 show the variations of lift coefficient, C_L, on a spherical droplet and a rigid sphere in a linear shear flow $\alpha = 0.0$, 0.1, 0.2, 0.3 and 0.4 against the particle Reynolds number, Re_p, respectively. The lift force in a uniform unsheared flow ($\alpha = 0.0$) does not appear ($C_L = 0$) in the case of either a spherical droplet or a rigid sphere. The values of C_L on a spherical droplet and a rigid sphere in a linear shear flow rapidly decrease with increasing Re_p in the moderate particle Reynolds-number range of $Re_p < 10$. In the high particle Reynolds-number range of $Re_p \geqslant 50$,

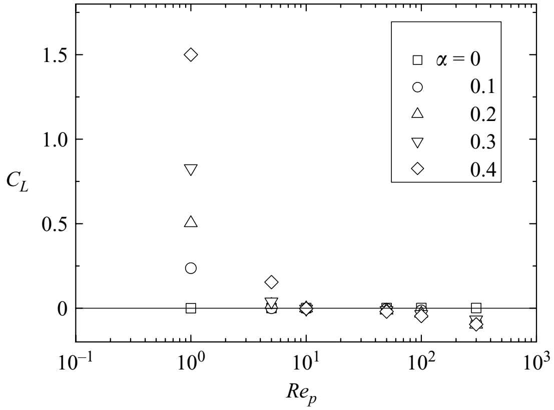

FIGURE 18. Lift coefficient, C_L, on a rigid sphere versus the particle Reynolds number, Re_p.

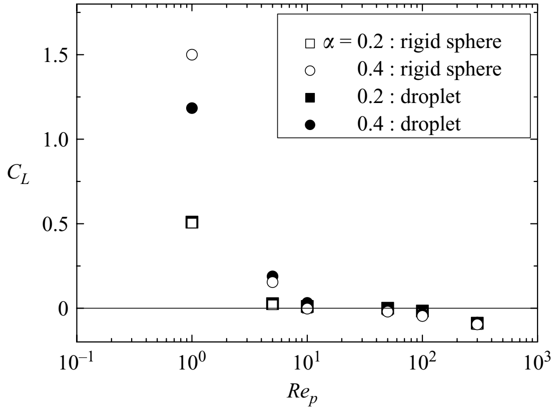

FIGURE 19. Lift coefficient, C_L, on a spherical droplet and a rigid sphere versus the particle Reynolds number, Re_p.

the computed C_L on a spherical droplet and a rigid sphere show small negative values. The effects of the shear rate α on C_L on a spherical droplet and a rigid sphere increase with increasing α. The behaviour of the lift force on a droplet is similar to that on a rigid sphere. Figure 19 shows comparisons of the lift coefficient, C_L, on a spherical droplet in a linear shear flow ($\alpha = 0.2$ and 0.4) with C_L on a rigid sphere in a linear shear flow ($\alpha = 0.2$ and 0.4). In the low-shear-rate case ($\alpha = 0.2$), there is no remarkable difference in C_L between a rigid sphere and a spherical droplet. However, in the high-shear-rate case ($\alpha = 0.4$), the value of C_L on a spherical droplet is much smaller than that on a rigid sphere at the low particle Reynolds number of $Re_p = 1$. On the other hand, Legendre & Magnaudet (1997) showed that in the small particle Reynolds-number region of $Re_p \ll 1$, the ratio of C_L on a water droplet to that on a rigid sphere is 0.987 irrespective of α. They derived this ratio by using Saffman's low-Reynolds-number theory that neglected the advection term of the equation of motion. However, the present result with a ratio of 0.790 for $\alpha = 0.4$ suggests that the low-Reynolds-number theory should not be used for estimating the lift force on a spherical droplet with $Re_p \geqslant 1$.

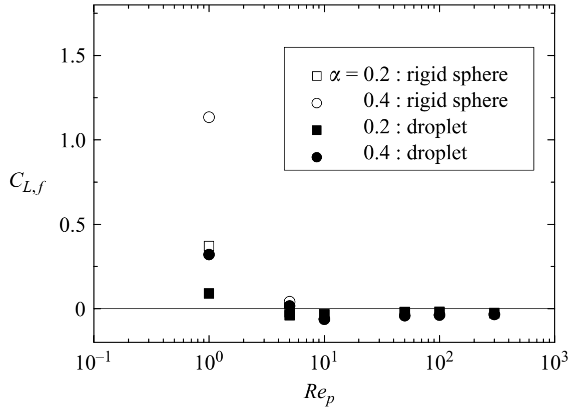

FIGURE 20. Viscous lift coefficient on a droplet and a rigid sphere, $C_{L,f}$, for $\alpha = 0.2$ and 0.4.

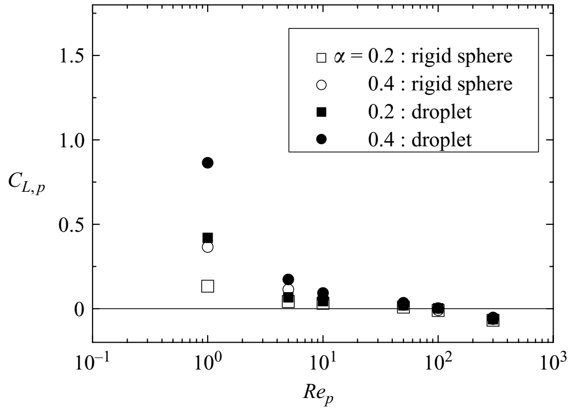

FIGURE 21. Pressure lift coefficient on a droplet and a rigid sphere, $C_{L,p}$, for $\alpha = 0.2$ and 0.4.

To clarify the effects of boundary conditions on the spherical surface on C_L, the viscous and pressure lifts, $C_{L,f}$ and $C_{L,p}$, acting on a spherical droplet are compared with those acting on a rigid sphere in figures 20 and 21, respectively. The value of the viscous lift coefficient, $C_{L,f}$, on a spherical droplet is smaller than that on a rigid sphere at the low particle Reynolds number of $Re_p = 1$. Figure 22 shows the surface contours of the y-component of the instantaneous viscous stress on the surface of a spherical droplet and a rigid sphere in a linear shear flow at $Re_p = 1$ and $\alpha = 0.4$ together with ambient velocity field and streamlines. The decrease of the viscous lift on a droplet can be understood from the decrease of the viscous lift in the upper part of the droplet. Figure 23 shows the velocity fields and streamlines outside and inside a spherical droplet in a linear shear flow at $Re_p = 1$ and $\alpha = 0.4$ on the centreplane ($z = 0$). Near the upper surface of the droplet, the direction of the water flow inside a spherical droplet is the same as the direction of the air flow outside a spherical droplet. Therefore, the decrease of viscous lift is caused by the tangential velocity on the droplet surface. On the contrary, the value of the pressure lift coefficient, $C_{L,p}$, on a spherical droplet is larger than that on a rigid sphere (figure 21). This can be explained from figure 24 which shows the surface contours of the y-component of the instantaneous pressure on the surface of a spherical droplet and a rigid sphere

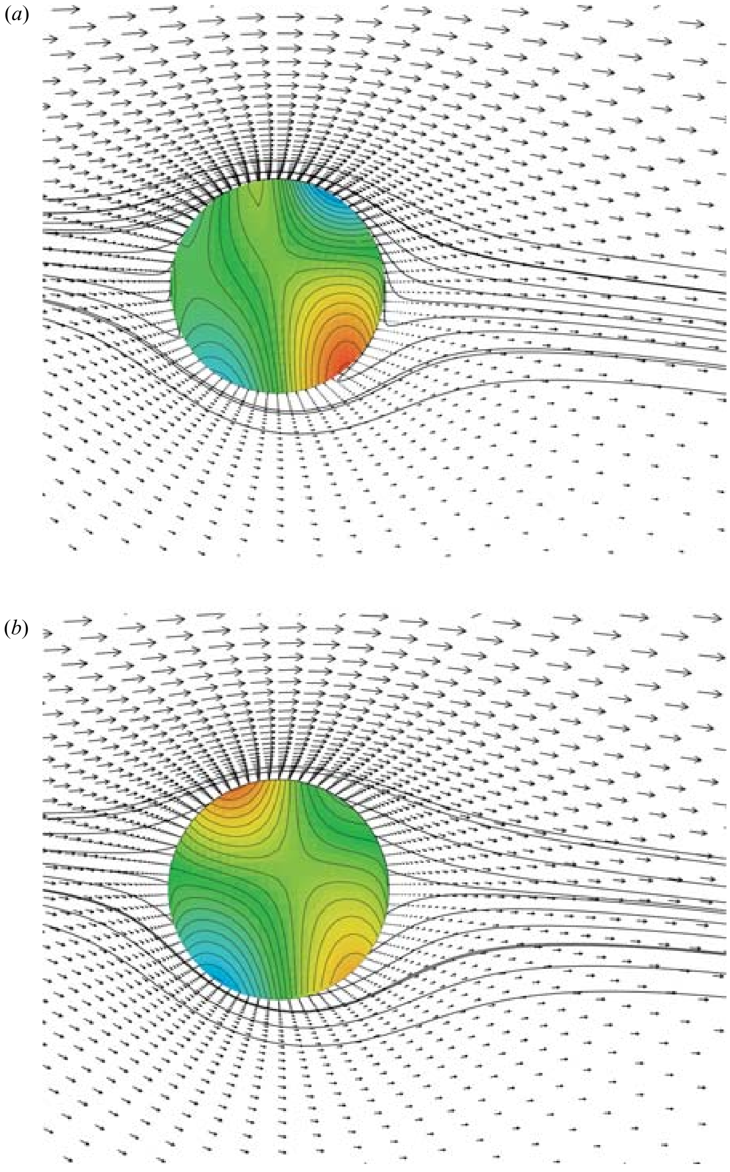

FIGURE 22. Surface contours of the y-component of the viscous stress acting on a droplet and a rigid sphere at $Re_p = 1$ and $\alpha = 0.4$ with ambient velocity field and streamlines: (a) droplet; (b) rigid sphere. The red and blue indicate high and low values of the viscous stress.

in a linear shear flow at $Re_p = 1$ and $\alpha = 0.4$ together with ambient velocity field and streamlines. That is, the tangential velocity on the droplet surface promotes the pressure difference between the higher fluid velocity side and the lower fluid velocity side.

4. Conclusions

A three-dimensional direct numerical simulation was first performed for a linear shear flow outside and inside a spherical droplet with a high particle Reynolds

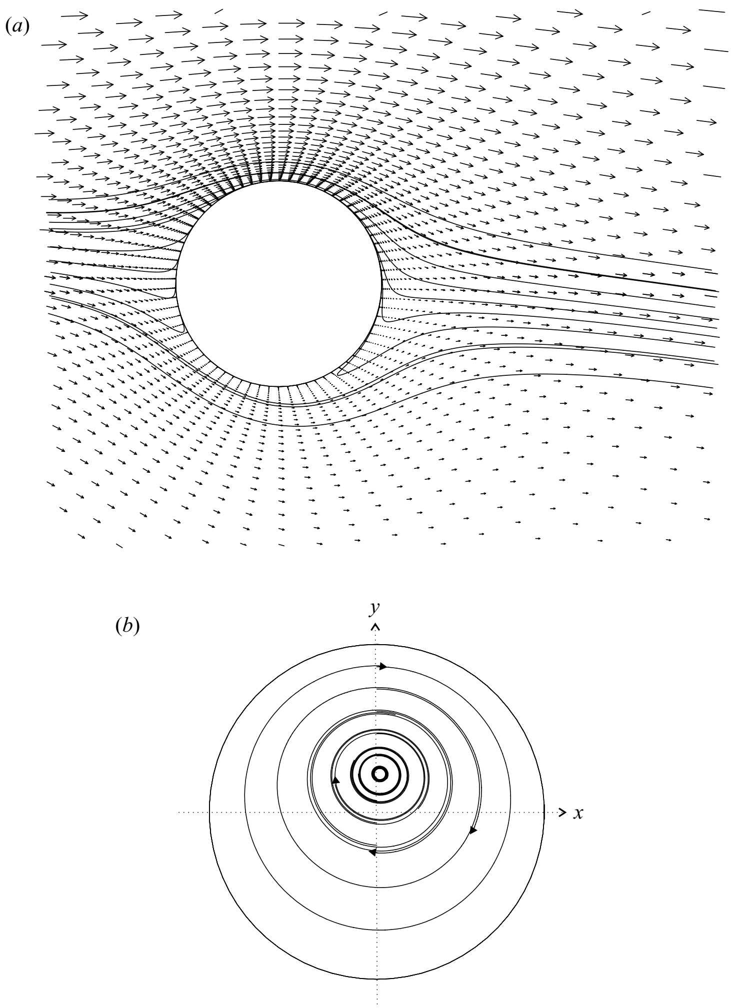

FIGURE 23. Velocity fields and streamlines at $Re_p = 1$ and $\alpha = 0.4$: (*a*) outside, (*b*) inside a spherical droplet.

number, and the effects of fluid shear on drag and lift forces were investigated by comparing it with the DNS predictions of a rigid sphere. The main results from this study can be summarized as follows.

The velocity field inside a droplet is not axisymmetric at high particle Reynolds numbers, and therefore a rough assumption of axial symmetry used in the previous studies is unacceptable.

The drag coefficient on a spherical droplet increases with increasing shear rate for a fixed value of the particle Reynolds number, and the dependence of the drag coefficient on the shear rate is more obvious for higher particle Reynolds numbers. The difference in the drag between a spherical droplet and a rigid sphere in a linear shear flow never exceeds 4 %, but the drag on a spherical droplet is a little smaller than that on a rigid sphere.

The lift coefficient on a spherical droplet decreases with increasing particle Reynolds number, and it acts from the high-speed side to the low-speed side in the linear shear flow with the high particle Reynolds number of $Re_p \geqslant 50$. The behaviour of the lift

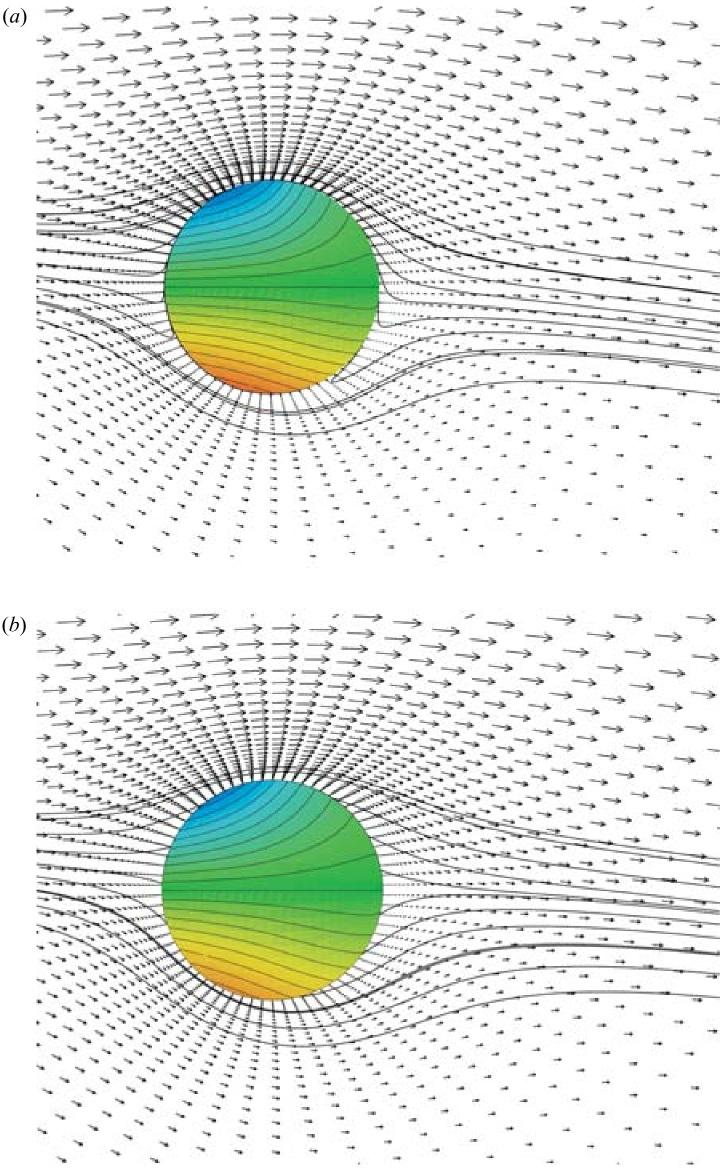

FIGURE 24. Surface contours of the y-component of the pressure acting on a droplet and a rigid sphere at $Re_p = 1$ and $\alpha = 0.4$ with ambient velocity field and streamlines: (*a*) droplet; (*b*) rigid sphere. The red and blue indicate high and low values of the pressure.

force on a spherical droplet is similar to that on a rigid sphere. In the low particle Reynolds-number region of $Re_p \approx 1$ with high shear rate, the lift force on a spherical droplet is smaller than that on a rigid sphere. The difference is attributed to the decrease of the viscous lift and the increase of the pressure lift on a spherical droplet that are caused by the water flow inside a spherical droplet.

This work was supported by the Japan Ministry of Education, Science and Culture through Grants-in-Aid (no. 14102016) and the 21st Century COE Program for Research and Education on Complex Functional Mechanical Systems. The computations were conducted by the supercomputer of the Centre for the Global Environment Research, National Institute for Environmental Studies, Environment Ministry of Japan. The authors thank Dr Shu Takagi, University of Tokyo, for his useful comments on the estimation of the lift force based on the low-Reynolds-number theory at the 2005 annual meeting of the Japan Society of Fluid Mechanics.

REFERENCES

Auton, T. R. 1987 The lift force on a spherical body in a rotational flow. *J. Fluid Mech.* **183**, 199–218.

Bagchi, P. & Balachandar, S. 2002 Effect of rotation on the motion of a solid sphere in linear shear flow at moderate *Re*. *Phys. Fluids* **14**, 2719–2737.

Beard, K. V. & Pruppacher, H. R. 1969 A determination of the terminal velocity and drag of small water drops by wind tunnel. *J. Atmos. Sci.* **26**, 1066–1072.

Chen, W. H. 2001 Dynamics of sulfur dioxide absorption in a raindrop falling at terminal velocity. *Atmos. Environ.* **35**, 4777–4790.

Clift, R., Grace, J. R. & Weber, M. E. 1978 *Bubbles, Drops and Particles*. Academic, San Diego, CA.

Dandy, D. & Dwyer, H. A. 1990 A sphere in linear shear flow at finite Reynolds number: effect of shear on particle lift, drag, and heat transfer. *J. Fluid Mech.* **216**, 381–410.

Gunn, R. & Kinzer, G. D. 1949 The terminal velocity of fall for drops in stagnant air. *J. Met.* 243–248.

Hanazaki, H. 1988 A numerical study of three-dimensional stratified flow past a sphere. *J. Fluid Mech.* **192**, 393–419.

Kawamura, T. & Kuwahara, K. 1984 Computation of high Reynolds number flow around circular cylinder with surface roughness. *AIAA Paper* 84-0340.

Komori, S. & Kurose, R. 1996 The effects of shear and spin on particle lift and drag in a shear flow at high Reynolds numbers. In *Advances in Turbulence VI* (ed. S. Gavrilakis, L. Machiels & P. A. Monkewitz), pp. 551–554, Kluwer.

Kurose, R. & Komori, S. 1999 Drag and lift force on a rotation sphere in linear shear flow. *J. Fluid Mech.* **384**, 183–206.

Kurose, R., Misumi, R. & Komori, S. 2001 Drag and lift forces acting on a spherical bubble in a linear shear flow. *Intl J. Multiphase Flow* **27**, 1247–1258.

Leal, L. G. 1980 Particle motions in a viscous fluid. *Annu. Rev. Fluid Mech.* **12**, 435–476.

LeClair, B. P., Hamielec, A. E., Pruppacher, H. R. & Hall, W. D. 1972 A theoretical and experimental study of internal circulation in water drops falling at terminal velocity in air. *J. Atmos. Sci.* **29**, 728–740.

Legendre, D. & Magnaudet, J. 1997 A note on the lift force on a spherical bubble or drop in a low-Reynolds-number shear flow. *Phys. Fluids* A **9**, 3572–3574.

Legendre, D. & Magnaudet, J. 1998 The lift force on a spherical bubble in a viscous linear shear flow. *J. Fluid Mech.* **368**, 81–126.

McLaughlin, J. B. 1993 The lift on a small sphere in wall-bounded linear shear flows. *J. Fluid Mech.* **246**, 249–265.

Mei, R. & Klausner, J. F. 1994 Shear lift force on spherical bubbles. *Intl J. Heat Fluid Flow* **15**, 62–65.

Morsi, S. A. & Alexander, A. J. 1972 An investigation of particle trajectories in two-phase flow system. *J. Fluid Mech.* **55**, 193–208.

Saffman, P. G. 1965 The lift on a small sphere in a slow shear flow. *J. Fluid Mech.* **22**, 385–400.

Sakamoto, H. & Haniu, H. 1995 The formation mechanism and shedding frequency of vortices from a sphere in uniform shear flow. *J. Fluid Mech.* **287**, 151–171.

Wohl, P. R. & Rubinow, S. I. 1974 The transverse force on a drop in an unbounded parabolic flow. *J. Fluid Mech.* **62**, 185–207.